Hurricane Directional Wave Spectrum Spatial Variation at Landfall

E. J. WALSH, C. W. WRIGHT, D. VANDEMARK, AND W. B. KRABILL

NASA Goddard Space Flight Center, Wallops Flight Facility, Wallops Island, Virginia

A. W. GARCIA

U.S. Army Engineer Research and Development Center, Vicksburg, Mississippi

S. H. HOUSTON,* S. T. MURILLO, M. D. POWELL, P. G. BLACK, AND F. D. MARKS JR.

NOAA/AOML Hurricane Research Division, Miami, Florida

(Manuscript received 30 March 2001, in final form 1 October 2001)

ABSTRACT

The NASA Scanning Radar Altimeter (SRA) flew aboard one of the NOAA WP-3D hurricane research aircraft to document the sea surface directional wave spectrum in the region between Charleston, South Carolina, and Cape Hatteras, North Carolina, as Hurricane Bonnie was making landfall near Wilmington, North Carolina, on 26 August 1998. Two days earlier, the SRA had documented the hurricane wave field spatial variation in open water when Bonnie was 400 km east of Abaco Island, Bahamas. Bonnie was similar in size during the two flights. The maximum wind speed was lower during the landfall flight (39 m s^{-1}) than it had been during the first flight (46 m s^{-1}). Also, Bonnie was moving faster prior to landfall (9.5 m s^{-1}) than when it was encountered in the open ocean (5 m s^{-1}). The open ocean wave height spatial variation indicated that Hurricane Bonnie would have produced waves of 10 m height on the shore northeast of Wilmington had it not been for the continental shelf. The gradual shoaling distributed the wave energy dissipation process across the shelf so that the wavelength and wave height were reduced gradually as the shore was approached. The wave height 5 km from shore was about 4 m.

Despite the dramatic differences in wave height caused by shoaling and the differences in the wind field and forward speed of the hurricane, there was a remarkable agreement in the wave propagation directions for the various wave components on the two days. This suggests that, in spite of its complexity, the directional wave field in the vicinity of a hurricane may be well behaved and lend itself to be modeled by a few parameters, such as the maximum wind speed, the radii of the maximum and gale force winds, and the recent movement of the storm.

1. Introduction

The hurricane data presented here were acquired through a joint effort between the National Aeronautics and Space Administration (NASA) Goddard Space Flight Center and the National Oceanic and Atmospheric Administration (NOAA) Atlantic Oceanographic and Meteorological Laboratory/Hurricane Research Division (HRD). The NASA Scanning Radar Altimeter (SRA) flew aboard one of the WP-3D hurricane research aircraft of the NOAA/Aircraft Operation Center. The SRA provided the first documentation of the spatial variation of the sea surface directional wave spectrum throughout a hurricane in open water. Those data were obtained on 24 August 1998, when Bonnie, a large Category 3 hurricane (Avila 1998), was 400 km east of Abaco Island, Bahamas (Wright et al. 2001).

This paper describes the first documentation of the directional wave spectrum throughout a hurricane making landfall as Bonnie was approaching Wilmington, North Carolina, on 26 August 1998. The NOAA aircraft height was about 2.2 km as the SRA documented the sea surface directional wave spectrum in the region between Charleston, South Carolina, and Cape Hatteras, North Carolina. The spatial variation of the sea surface directional wave spectrum during hurricane landfall is detailed and contrasted with the spatial variation observed while Bonnie was in the open ocean (Wright et al. 2001). The great similarity of its components on the two days suggests that the directional wave spectrum

* Current affiliation: National Weather Service Forecast Office, CPHC/NOAA, Honolulu, Hawaii.

Corresponding author address: Edward J. Walsh, NOAA Environmental Technology Laboratory, R/ETL1, 325 Broadway, Boulder, CO 80305-3328.
E-mail: walsh@osb.wff.nasa.gov

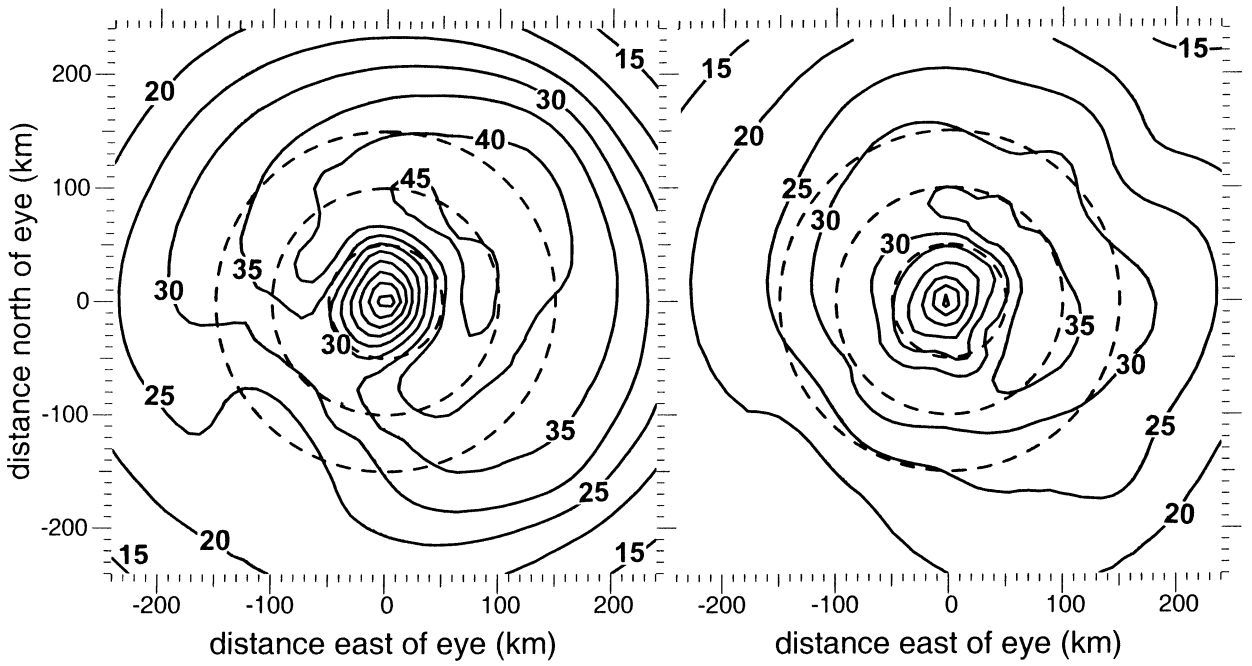

FIG. 1. Contours of wind speed (m s^{-1}) for Hurricane Bonnie from the HRD surface wind field analyses corresponding to the open ocean flight (left panel) and the landfall flight (right panel).

in the vicinity of a hurricane may be well behaved and lend itself to be modeled by a few parameters.

2. Comparison of wind speed and wave height in the open ocean and at landfall

The preliminary HRD wind fields were generated for the landfall of Bonnie following the methods outlined by Powell et al. (1996). The input observations were similar to those used for Bonnie over deep water in Wright et al. (2001), except surface observations from fixed marine and coastal platforms were available.

Figure 1 compares the HRD surface wind field analysis corresponding to the open-ocean flight (left panel) with that for landfall (right panel). The radius of maximum wind and general wind speed variation were quite similar. The main difference in the two wind fields was that the maximum mesoscale surface wind speed was 39 m s^{-1} at landfall, about 15% lower than the 46 m s^{-1} value determined two days earlier over the open ocean. The distribution of the highest winds is also shifted about 20° or 30° clockwise at landfall relative to the open ocean distribution, possibly due to the faster forward motion of the storm.

Figure 2 shows a portion of the North and South Carolina shoreline with the solid curve indicating the track of Bonnie prior to landfall. The interpolated eye positions are shown at 5-h intervals relative to the first eye penetration by the NOAA aircraft. The dotted curve shows the track of Bonnie during the open ocean flight, shifted geographically to make the first eye penetration coincident with that of the landfall flight. During the 10-h interval between 15 h and 5 h prior to the first eye penetration, Bonnie was moving about 5 m s^{-1} with a mean track 330° in the open ocean, but prior to landfall it moved at about 9.5 m s^{-1} with a mean track of 334°. Then Bonnie's speed began to increase when it was in

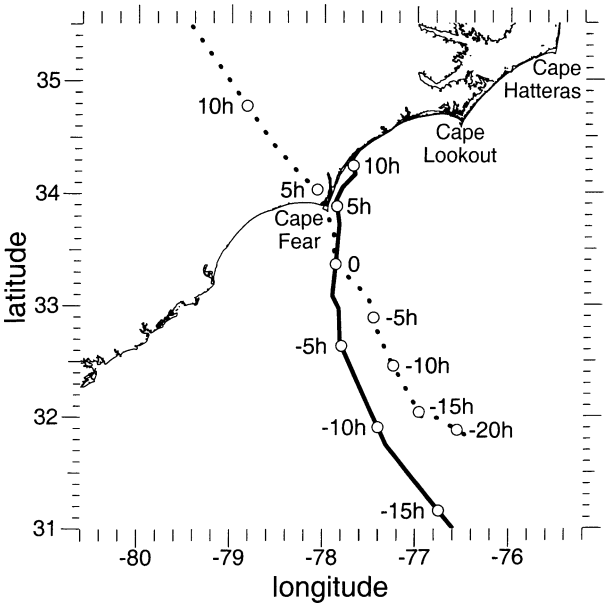

FIG. 2. North and South Carolina shoreline with the track of Hurricane Bonnie prior to landfall on 26 Aug 1998 (solid curve). The dotted curve shows the track of Bonnie during the open-ocean flight on 24 Aug, shifted geographically to make the first eye penetration by the NOAA aircraft coincident with that of the landfall flight.

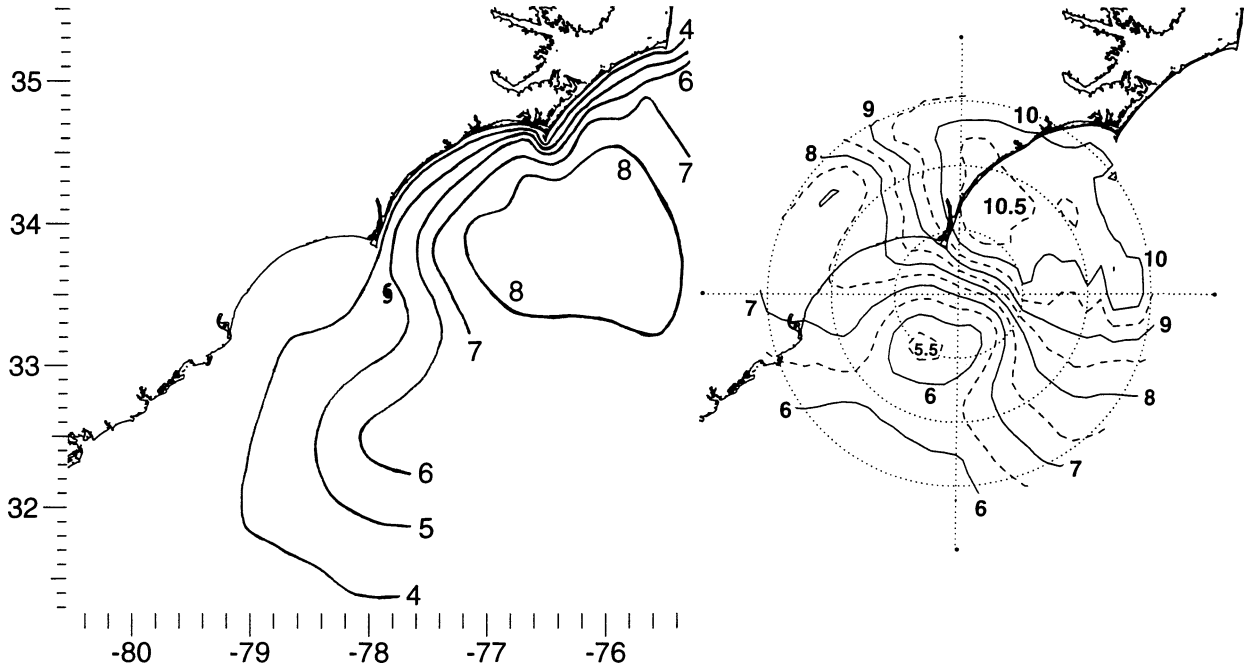

FIG. 3. North and South Carolina shoreline with contours of significant wave height H_S at landfall corresponding to the Hurricane Bonnie eye location indicated by the hurricane symbol (left panel) and contours of Bonnie H_S in the open ocean (right panel) superimposed on the Carolina shoreline using the same eye location indicated on the left panel. The dashed contours in the right panel are halfway between the integer meter solid contours.

open ocean (dotted curve) and decrease when it was approaching land (solid curve).

Donelan et al. (1992) measured the differential wave growth between towers arranged in a line in Lake St Clair and developed an expression that provided a smooth transition from rapidly growing short fetch waves to the asymptotic invariant state of full development. This is rather more satisfying than the traditional expressions of nondimensional wave energy being proportional to nondimensional fetch raised to a power, with an abrupt transition to the fully developed state. The Donelan et al. (1992) expression developed from the Lake St Clair data fit the Joint North Sea Wave Project (JONSWAP) field data better than the JONSWAP power law (Hasselmann et al. 1973), and it reduced to essentially the JONSWAP expression for linear growth rate of nondimensional wave energy with nondimensional fetch at the shorter fetches. The JONSWAP power law can be rearranged into the form

$$H_S = 0.0016\ (g^{-1} F)^{0.5}\ U_{10}, \qquad (1)$$

where F is the physical fetch and U_{10} is the wind speed at 10-m height.

In hurricanes, the highest wind speeds are generally associated with nondimensional fetches in the linear growth rate region because of the curvature of the wind field. Then (1) indicates that, for a fixed physical fetch, wave height would be proportional to wind speed.

Since Bonnie was similar in size during the two flights, the curvature of the wind field and fetch in the vicinity of the radius of maximum wind would be similar. With a 15% reduction in the maximum mesoscale surface wind speed at landfall, a similar reduction in the maximum wave height would be expected. However, the higher translation speed prior to landfall would tend to increase the wave height. The open ocean translation speed of 5 m s^{-1} matched the group velocity of waves of length 65 m, and the faster waves at the peak of the spectrum would outdistance the storm soon after they were generated. The 9.5 m s^{-1} translation speed prior to landfall matched the group velocity of 230 m waves, significantly increasing the effective fetch and duration of waves near the peak of the spectrum which moved in the direction of translation of the storm (Bretschneider 1957; Shemdin 1980; Young 1988; MacAfee and Bowyer 2000a,b; Bowyer 2000).

The left side of Fig. 3 shows the North and South Carolina shoreline with contours of significant wave height, H_S (4 times rms surface elevation), corresponding to the eye location indicated by the hurricane symbol at about 33.5°N, 77.8°W. The contours were determined from the SRA measurements in a subjective manner. The SRA wave height values were plotted in positions that were shifted spatially from the observation locations according to the relative vector between the eye position at the reference time and the observation time. Radials were drawn from the shifted values to the measurement locations, so an assessment could be made as to whether the wave height variation should have been associated with the location corresponding to the ref-

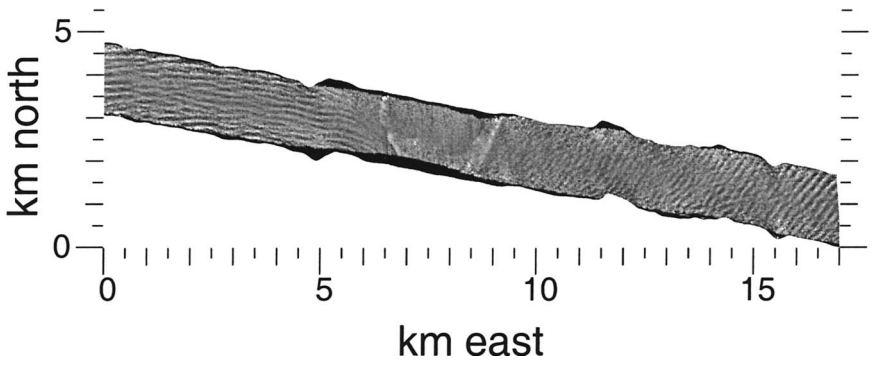

FIG. 4. Grayscale-coded topographic map produced from about 700 SRA raster scan lines as the aircraft crossed Cape Lookout during the landfall flight. The land mass occupies the region between about 6.5 and 9 km along the abscissa.

erence time or to the bathymetry. The H_S contours were then drawn free hand. They should not be taken as exact, but represent the general spatial variation of the wave height to provide a context for the detailed analysis which follows. The maximum wave height might have been over 9 m, but there were no data near the center of the 8 m contour.

On the right side of Fig. 3 the contours of H_S measured when Hurricane Bonnie was in the open ocean (Wright et al. 2001) are superimposed on the Carolina shoreline using the same eye location indicated on the left side of Fig. 3. The open ocean wave height variation suggests that, if the water had not been shoaling, the maximum wave height would had occurred on the shoreline in the region northeast of Wilmington. This is in dramatic contrast to the observations, which show the wave height diminishing to half its maximum value as the shore is approached. The gradual shoaling caused the energy to dissipate as the waves crossed the continental shelf (Shemdin et al. 1978; Tolman 1994; Young and Gorman 1995; Hwang et al. 1998; Ardhuin et al. 2001).

3. SRA wave topography measurements

The SRA scans a 1° (two-way) beam through the nadir point in the vertical plane that contains the aircraft wings and measures the range to 64 points over a swath width equal to 0.8 times the aircraft height. In real time, the slant ranges are multiplied by the cosine of the off-nadir incidence angles (including the effect of aircraft roll attitude) to determine the vertical distances from the aircraft to the sea surface. These distances are subtracted from the aircraft height to produce a sea-surface elevation map, which is displayed on a monitor in the aircraft to enable real-time assessments of data quality and wave properties. The scan rate was 8 Hz during the Bonnie flight. (It is presently 10 Hz, and faster scan rates are possible.)

Figure 4 shows a grayscale-coded topographic map produced from about 700 SRA scan lines as the aircraft crossed Cape Lookout (34.58°N, 76.53°W) during the landfall flight. The aircraft flight direction was from right to left. The wave topography shows a dramatic spatial variation in the wave field with the waves propagating toward the northwest on the east side of Cape Lookout, and toward the north on the west side.

Figure 5 shows five contiguous 10-km segments of SRA gray-scale-coded topography on a different flight line as the NOAA aircraft headed north toward Cape Hatteras (35.27°N, 75.44°W). The waves were just starting to ''feel'' the ocean floor at the beginning of this dataset, and the water depth decreased along the track. The waves were initially propagating toward about 335°. As the waves approached the shore, the wavelength shortened, the amplitude decreased, and the propagation direction turned toward the north and finally northeast. The surf zone began at about 6.3 km up from the bottom of the right 10-km segment. The tip of Cape Hatteras is apparent at the top of the same segment.

4. Directional wave spectra

The SRA has a long heritage of measuring the energetic portion of the sea surface directional wave spectrum (Walsh et al. 1985, 1989, 1996). To obtain the wave spectra used in this paper, sea-surface topography from 180 cross-track scan lines of the SRA was interpolated to a north- and east-oriented 256 by 256 square grid of 7-m spacing centered on the data. The nominal along-track distance covered by the 180 scan lines was 2.7 km at the 8-Hz scan rate and 120 m s^{-1} nominal air speed. Only 119 of the 180 scan lines would fit within the 1785 m by 1785 m span of the grid if the aircraft were flying north or east, and even fewer if the aircraft had a tail wind, which was generally the case.

At the nominal aircraft height of 2.2 km for the landfall flight, the SRA swath width of 1760 m approximately matched the width of the square grid. If the aircraft were flying at a significant angle to the grid axes, some points near the cross-track corners of the grid would be empty.

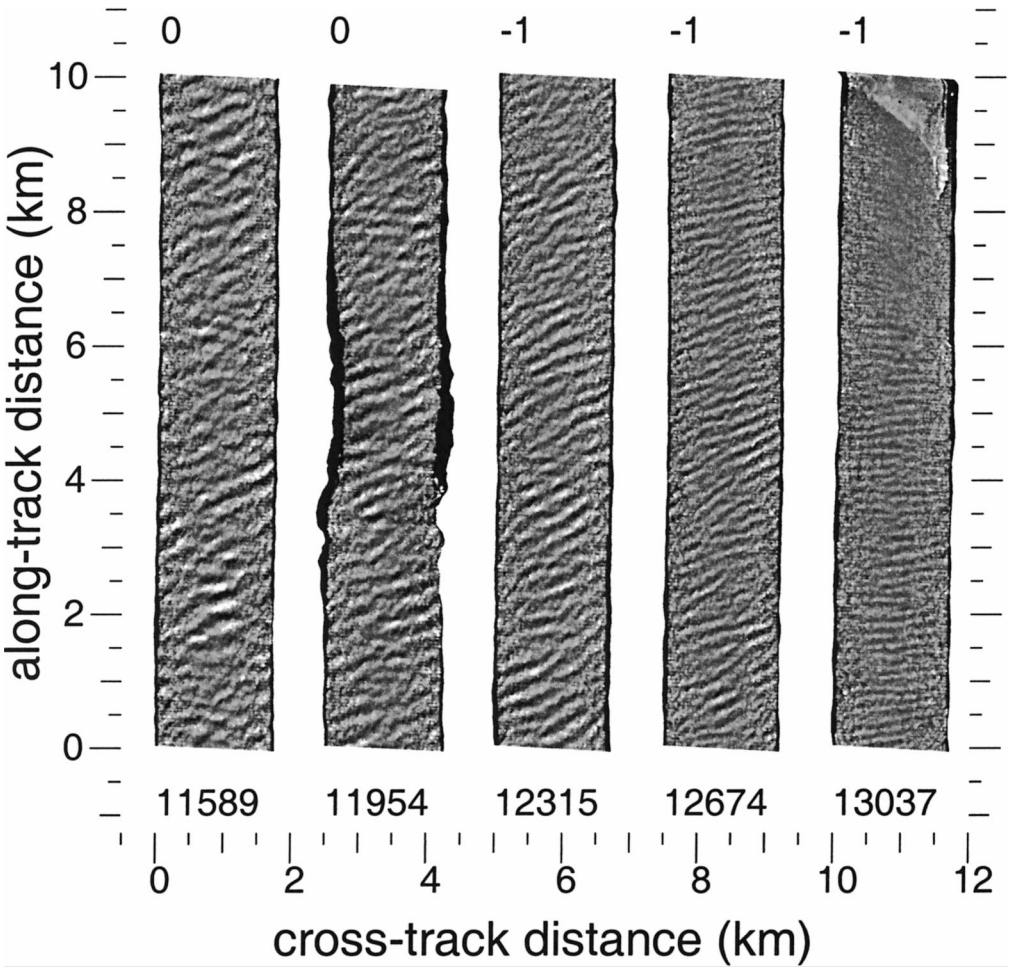

FIG. 5. Five contiguous 10-km segments of SRA grayscale-coded topography as the NOAA aircraft headed north toward Cape Hatteras. Time increases up the page and from left to right. The average aircraft track angle in degrees is indicated above each 10-km segment, and the starting scan line number (sln) is indicated below.

The elevations in the uniform grid were transformed by a two-dimensional fast Fourier transform (FFT). A filled grid would produce north and east wavenumber spectral resolutions of 0.0035 rad m^{-1}. The starting scan line number for each succeeding spectrum was advanced by 100. For the spectra used in this paper, five adjacent individual spectra were averaged and then smoothed with a 3 by 3 uniform weighting filter spanning 0.01 rad m^{-1} in wavenumber space. The result approached 90 degrees of freedom. The artifact spectral lobes were deleted, and the real lobes were Doppler corrected. Wright et al. (2001) describes these processes in detail.

Figures 6 through 10 show 5-spectra averages of the wavenumber directional wave spectra generated from SRA topography measured in Hurricane Bonnie during landfall. The time sequence progresses from left to right, and top to bottom in each figure. The 75 spectra indicate the directions in which the wave energy is propagating. They span almost 6 h of data and have been selected to provide detailed information on all the various spectral shapes observed. They provide an opportunity to assess the value judgments made in partitioning the spectra into wave components and a context for the plan view maps of the spatial variation of the wave field components.

For the open ocean analysis (Wright et al. 2001), the limits on the portion of the spectra displayed were symmetrical on both north and east axes, ± 0.07 rad m^{-1}. In this paper, the limits are asymmetrical, extending farther to the south and the east to accommodate the shorter wavelengths observed in those directions.

Each of Figs. 6–10 contains 15 spectra. The starting spectrum number for the 5-spectra averages used in this paper was always incremented by five, so the spectral averages never overlap, although there was a slight overlap at the beginning and end of the topographic data used to generate adjacent 5-spectra averages.

The small circles on the map in the upper left panel of each figure show the spectral locations relative to the Carolina coastline and the north wall of the Gulf Stream.

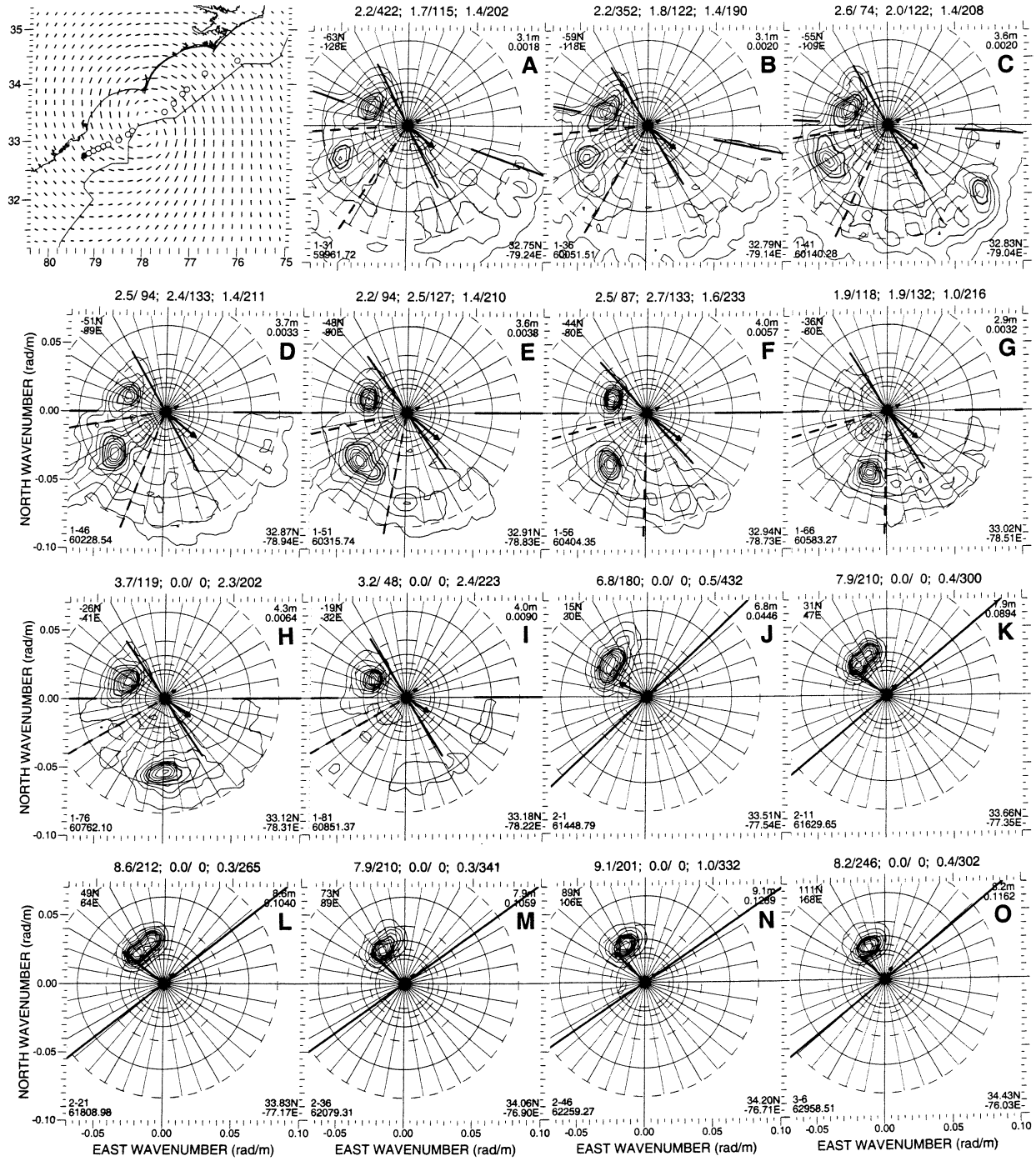

FIG. 6. SRA directional wave spectra acquired between 1639 and 1729 UTC 26 Aug 1998. The map in the upper left panel shows part of the North and South Carolina shoreline and the northern boundary of the Gulf Stream. The 15 circles indicate the locations of the 15 spectra, and the circle corresponding to the first spectrum in the sequence is filled. The short lines on the map extend in the downwind direction a length proportional to the speed given by the HRD surface wind analysis for the eye location corresponding to the time of the 8th of the 15 spectra shown. A wind speed of 30 m s^{-1} corresponds to a length of 0.1° of latitude. The directional wave spectra reference wave propagation directions and the dashed circles (outer to inner) correspond to wavelengths of 75 m, 150 m, 250 m, and 350 m. The solid circles indicate wavelengths of 100 m, 200 m, and 300 m. The arrowhead at a distance 0.01 rad m^{-1} from the spectral origin points in the aircraft flight direction. The thick arrow extends in the downwind direction a distance proportional to the HRD surface wind vector at that spectral location. A wind speed of 30 m s^{-1} corresponds to a length of 0.03 rad m^{-1}.

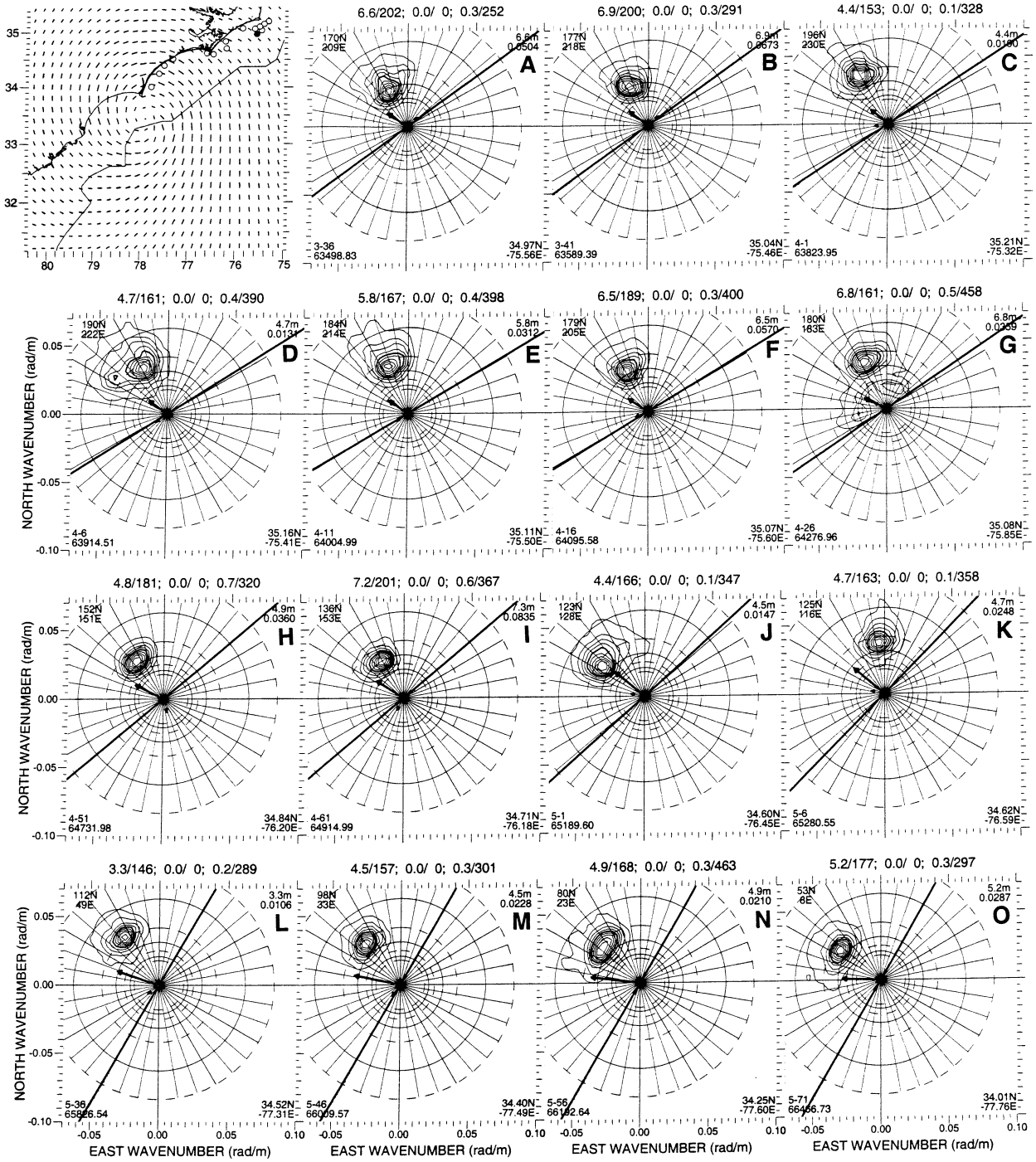

FIG. 7. SRA directional wave spectra acquired between 1738 and 1828 UTC 26 Aug 1998 in the same format as Fig. 6.

The circle corresponding to the first spectrum in the sequence is filled. The piecewise-linear approximation of the north wall of the Gulf Stream was determined by points extracted from the 26 August 1998 Oceanographic Features Analysis of the Naval Oceanographic Office. The boundary location may be uncertain. The Johns Hopkins University Applied Physics Laboratory (http://srbdata.jhuapl.edu/d0043/avhrr/gs_s/averages/98aug) image of the AVHRR observations between 0958 UTC 26 August and 2353 UTC 28 August 1998 indicated that almost no data were available in the Gulf Stream region between 32.2°N and 36°N due to cloud cover.

The total H_S is in the upper right corner of each spectrum. There are nine contours, linearly spaced from 10%

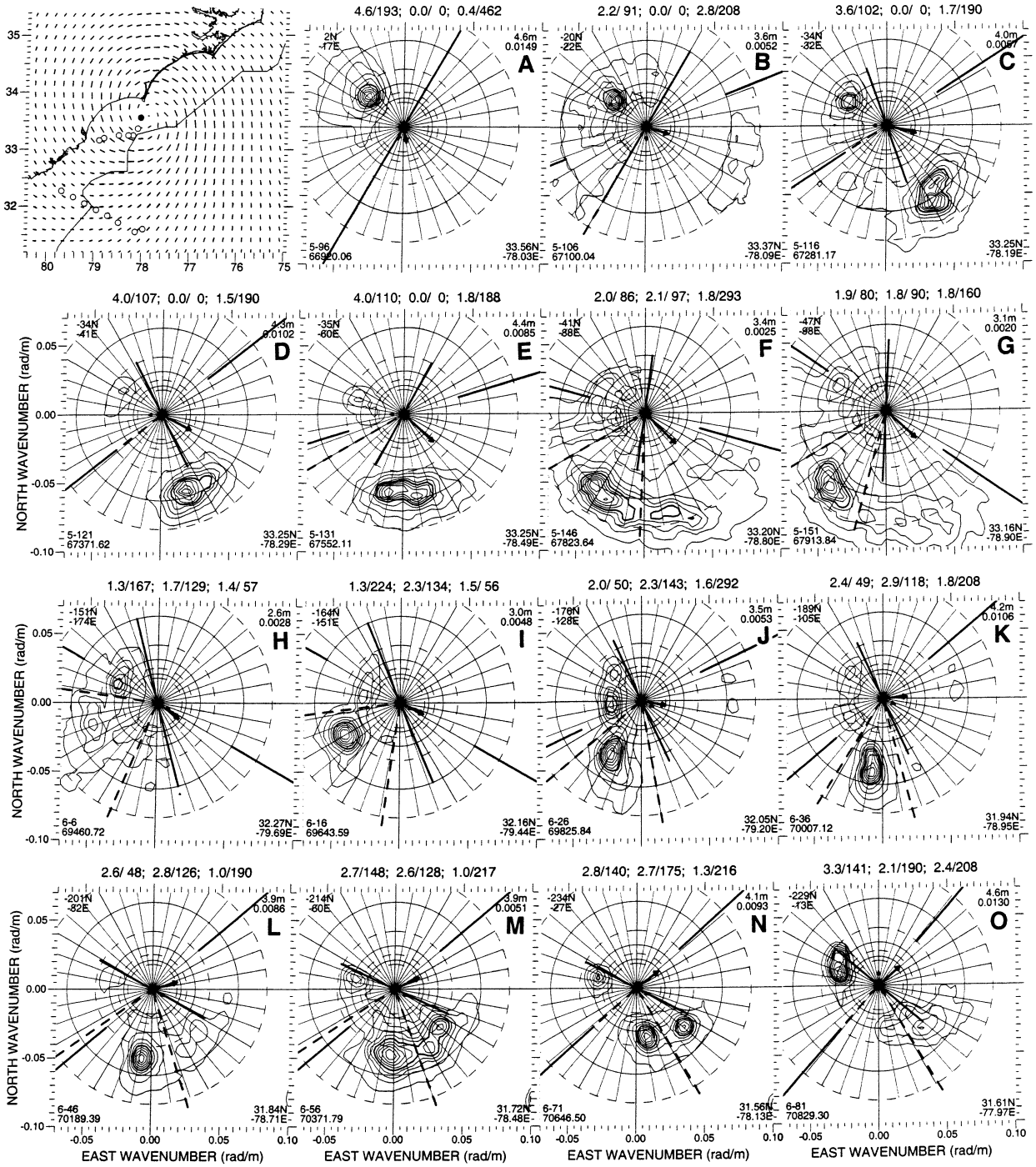

FIG. 8. SRA directional wave spectra acquired between 1835 and 1941 UTC 26 Aug 1998 in the same format as Fig. 6.

to 90% of the peak spectral density of each spectrum, which in (m^4 rad^{-2}) equals the number below the H_S in the upper right corner times 81 342. The north and east distances from the eye, in km, are indicated in the upper left corner, and the latitude and longitude are in the lower right corner of each spectrum. The lower left corner contains the flight segment and the starting spectrum number of the 5-spectrum average, separated by a hyphen, and the UTC seconds of the day (sod).

The thick radials on the spectra of Figs. 6 through 10 indicate the orientations of the boundaries of the half-planes used to eliminate the spectral artifact lobes. To be able to deal with complex situations (such as real spectral lobes in opposite half planes), there are separate

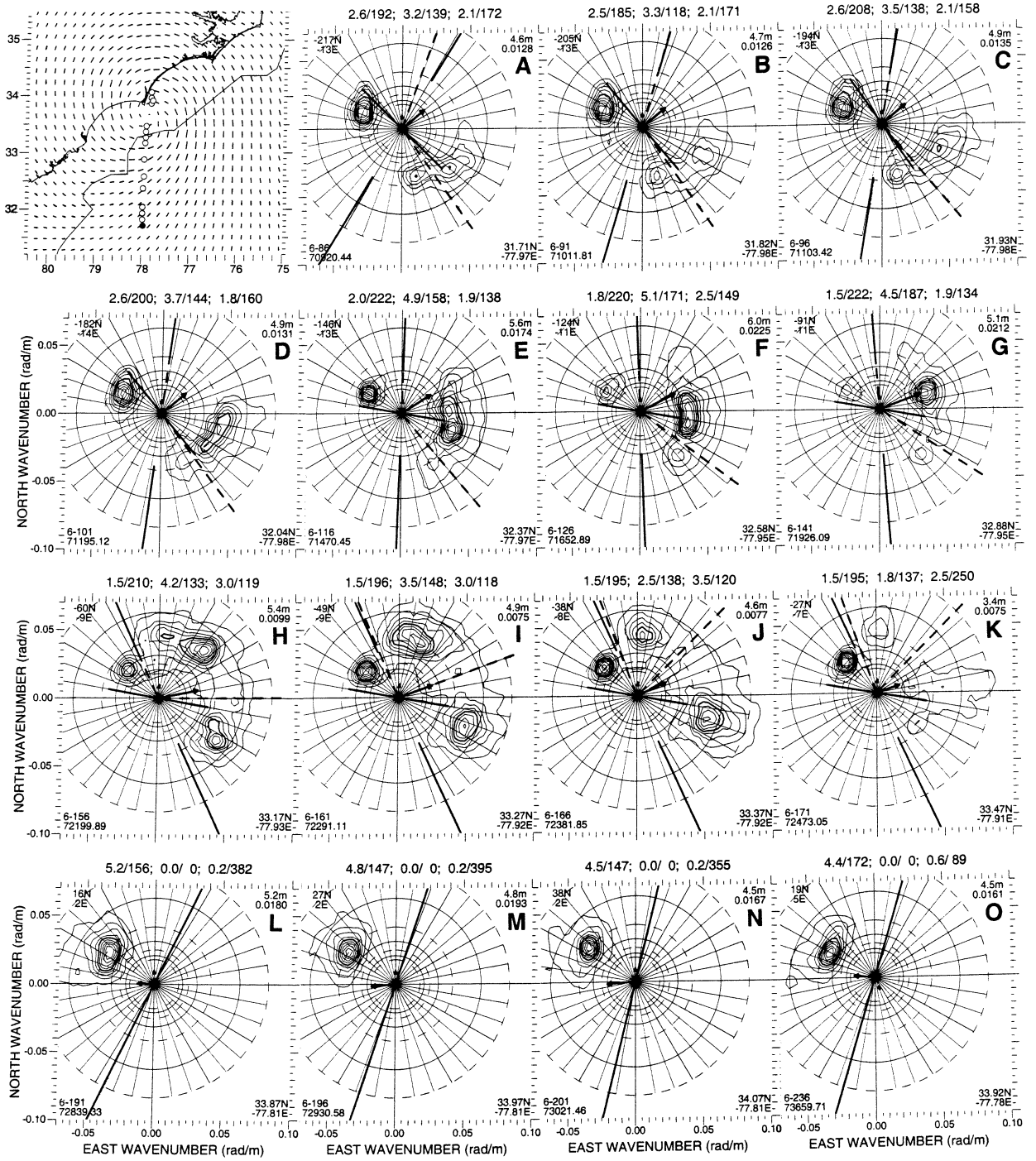

FIG. 9. SRA directional wave spectra acquired between 1942 and 2028 UTC 26 Aug 1998 in the same format as Fig. 6.

half-plane boundaries for wavelengths less than and greater than an arbitrary value, which varied between 75 and 200 m depending on the characteristics of the particular spectrum. The inner and outer half planes frequently have the same orientation. All spectral energy is deleted on the artifact side of each boundary, although subsequent Doppler corrections sometimes push the contours past the boundaries.

Two dashed radials were used to partition some of the spectra into two or three components. The three pairs of numbers, separated by a slash in the header of each spectrum, are the H_S and the wavelength at the spectral

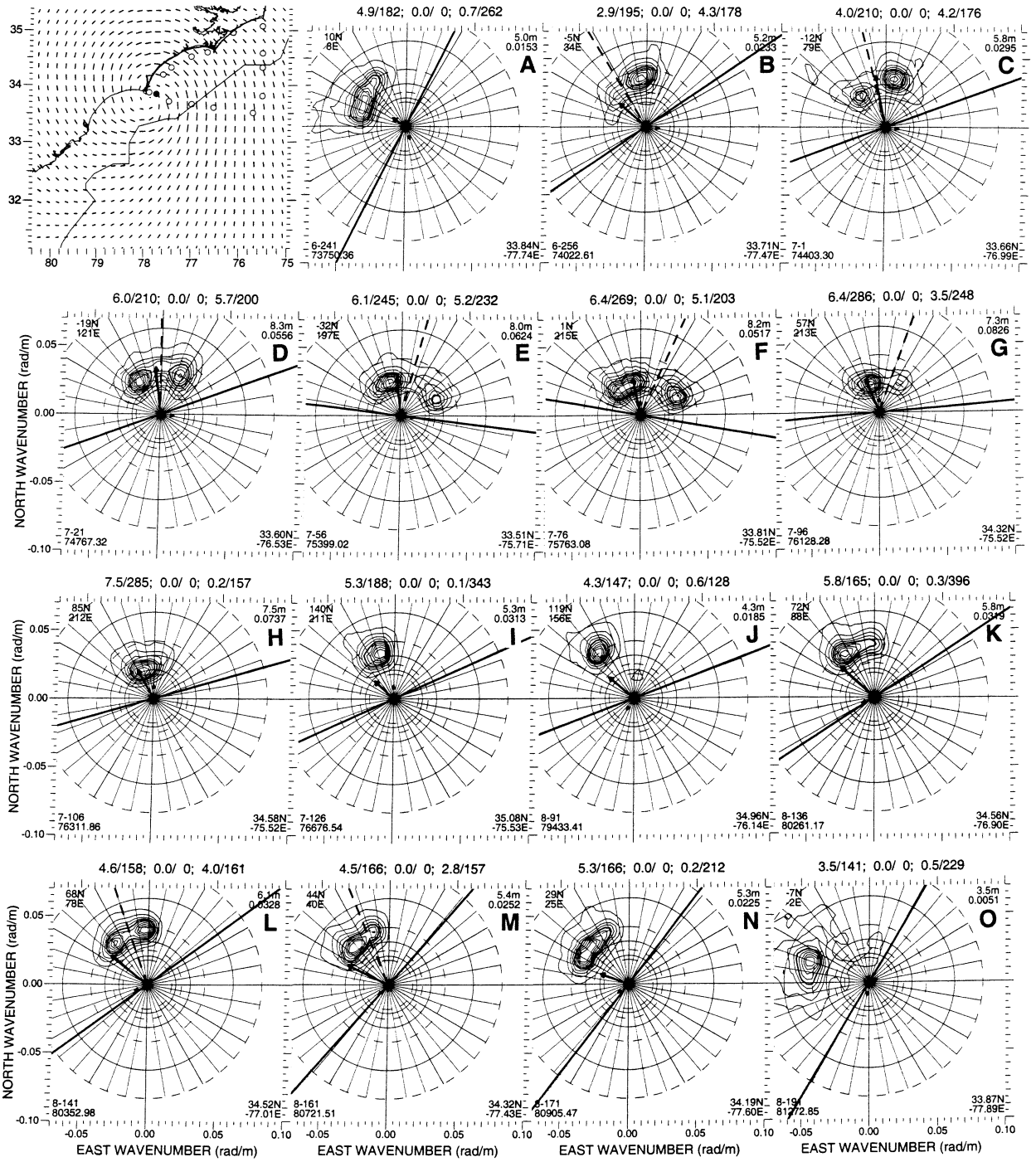

FIG. 10. SRA directional wave spectra acquired between 2029 and 2235 UTC 26 Aug 1998 in the same format as Fig. 6.

peak for each partition. The sequence of the three sets of numbers is in clockwise (CW) order around the spectrum. The square root of the sum of the squares of the partition wave height values in the header equals the total H_S in the upper right corner of each spectrum.

When only two wave components were identified, the two dashed radials were placed coincident between them so there appears to be only one and the middle elements in the header are zero. When only one component was identified, the two dashed radials were placed coincident at one of the half-plane boundaries and are not visible. In this case, some spurious numbers still show up in the third header position. As subjective as the partitioning process is, it can be valuable in examining and

comparing the general spatial variation of the complex wave fields associated with hurricanes.

The angles of the partition boundaries are decided upon for the times associated with a subset of the spectra. The partition boundary orientations for each spectrum are then obtained by linear interpolation in time. The same technique is applied to orient the half-plane boundaries used to delete the artifact spectral lobes.

5. Spectrum spatial variation and partitioning judgments

This section points out the wave field spatial variation in evidence in the spectra of Figs. 6–10 and discusses the subjective judgments made in determining the number and orientations of the dashed radials used to partition them into spectral components.

The SRA is not a perfect instrument and neither is the processing. The spectral energy was set to zero near the origin, but at times, contamination just outside that region produced an undesirable value for the partition wavelength in the spectral headers. The automatic determination of wavelength using the peak spectral density produced wavelengths of 422 and 352 m for the wind-driven component in the first partitions of Figs. 6a and 6b, instead of the 70-m values that would have been chosen subjectively.

The first pass through the eye was almost parallel to the coast. West of the eye (Figs. 6a–i), the wave field was trimodal, with a total H_S of 3–4 m. East of the eye, the wave field appeared unimodal (Figs. 6j–o) with an H_S of 7–9 m.

West of the eye, the spectral component in the middle partition showed significant spatial variation in propagation direction, from 243° in Fig. 6a to 178° in Fig. 6h, 95 km away. This swell was likely generated in the vicinity of the radius of maximum wind. The propagation direction at the observation points depends on the tangent to that radius for an earlier position of the storm given by the transit time for the wavelength observed.

Most of the SRA data loss is due to heavy rain. The spectral and H_S values in Fig. 6g are in error because half of the topographic data used to generate the five spectra in that average was obliterated by rain. The spectrum was included because it still showed the smooth progression of the propagation direction of the middle wave component.

A second dashed partition might have been placed in Figs. 6h and 6i in the vicinity of 130°. But that was very close to the downwind direction and did not seem reasonable. Adding or deleting partitions can cause abrupt changes in the component H_S values. In Fig. 6f, the H_S values for the first two components (CW) are 2.5 and 2.7 m. Their combined value is 3.7 m, the same as for the first component in Fig. 6h, where the partition separating the two components in Fig. 6f was removed.

A northwest propagating swell of wavelength about 200 m appeared throughout the flight line shown in Fig. 6. West of the radius of maximum wind, the northwest swell height was about 1.5 m. It grew rapidly in the eye and was over 8 m east of the eye.

East of the eye (Figs. 6j–o), the wave field appeared unimodal. The highest value of H_S was 9.1 m (Fig. 6n) with a dominant wavelength of 201 m. Banner et al. (2000) suggests that about 16% of the dominant waves would be breaking under these conditions.

Further to the east and closer to shore (Figs. 7a,b), the wavelength was still about 200 m, but the wave height diminished to under 7 m. There were spatial gradients in wave height both parallel to and perpendicular to the shore in this region near Cape Hatteras. When the aircraft reversed flight direction and traveled toward the southwest, the H_S increased from 4.4 to 6.5 m in just 30 km (Figs. 7c–f). Comparing Fig. 7a with 7f and Fig. 7b with 7e indicates reductions in both wave height and wavelength toward shore.

All the spectra in the right forward quadrant of the hurricane shown in Fig. 7 appear to be unimodal swell propagating toward the northwest. The biggest change in propagation direction occurred in the 12 km distance between the observation in Fig. 7j (306°) and Fig. 7k (353°), caused by the bathymetry in the vicinity of Cape Lookout (Fig. 4).

The shortest wavelength and lowest wave height in Fig. 7 occurred in the spectrum closest to the shore (Fig. 7l), and there was a monotonic increase in wavelength (146 m, 157 m, 168 m, 177 m) and H_S (3.3 m, 4.5 m, 4.9 m, 5.2 m) in the last four spectra of Fig. 7 as the distance from shore increased. All of these waves were significantly lower and shorter than the waves of 8–9 m height and 200 m wavelength seen farther from shore (Figs. 6k–n).

The second largest cause of SRA data loss is aircraft roll maneuvers. Shortly after the spectrum of Fig. 6i, the SRA data were corrupted by a series of aircraft roll maneuvers that were used to locate the eye. The spectrum in Fig. 7g shows evidence of low-frequency contamination caused by an aircraft roll maneuver. This type of contamination could be edited out on a case by case basis, but would require considerable effort. With a goal of processing the SRA data into directional wave spectra onboard the aircraft in near realtime to make the information available to the forecasters at the National Hurricane Center (NHC), some minor discrepancies need to be tolerated initially. Advanced processing techniques may eventually be able to edit all contaminated data.

Figure 8 shows wave spectra from the left rear quadrant of Bonnie. The most complex spectra generally occur in the rear half of the hurricane. The wave spectra in the right forward quadrant generally appear unimodal because the peak spectral densities are so high and the spectral contours only go down to the 10% level relative to the peak.

The sequence of spectra in Figs. 8a, 8b, and 8c dem-

onstrates the arbitrary nature of some decisions made in processing the data. In Fig. 8a, the decision was made that there was no real spectral energy in the right half plane. The location was near shore, and the wind was relatively light. In Fig. 8c, a significant wave component propagating toward the southeast was identified. Where that component first appeared is unclear, but it was arbitrarily assumed to be present in Fig. 8b at wavelengths of 100 m or shorter.

Once identified, the behaviors of the wave components are generally quite clear, such as the CW rotation and extending tail on the southeast wave component of Fig. 8c in the Figs. 8d–g sequence. It is when the wave components first begin to appear in the spectra that the uncertainty and arbitrariness generally occur.

The spectra shown in Figs. 8h–n, from the flight line about 150 km south of the Figs. 8c–g flight line, evidence a southward-propagating swell that rotates counterclockwise (CCW) along the flight line. This is because the flight direction was eastward instead of westward. The south propagating wave components rotate CW as the observation location moves west on both flight lines.

The average wavelength on the southern flight line is considerably longer than on the northern flight line, about 130 versus 100 m. But the longer wavelength on the southern flight line should not be thought of as evolving from shorter wavelength system on the northern flight line. The intervening wind at the observation time was either at right angles to or somewhat opposing the wave propagation directions. The transit time for 150 km at the 7.1 m s^{-1} group velocity of 130 m waves would be almost 6 h and the hurricane moved about 100 km in that time. The shorter wavelength on the northern flight line was due to fetch-limiting of the wave growth caused by the Carolina shoreline. When the waves observed on the southern flight line were generated, the hurricane was further to the south and there was less fetch-limiting.

Figure 9 shows a wave field curiosity. In the vicinity of the Gulf Stream northern boundary (Figs. 9h–j) there appear to be waves propagating in every direction in the northeast half plane except the downwind direction, despite its 20–30 m s^{-1} magnitude. There were certainly waves propagating in the downwind direction, but their spectral densities were not high enough to be prominent in these normalized spectra. It was decided not to use log instead of linear contours to extend below the 10% level relative to the peak spectral density because it made many of the spectra busy and difficult to interpret.

Figures 9 and 10 show additional examples of the subjective aspect of spectrum partitioning. The spectra of Figs. 9l–n are unimodal. The spectrum of Fig. 9o begins to be stretched in a CW direction, and that process continued in Fig. 10a, but no partition was used. Figures 10c–g were clearly bimodal; Fig. 10b was partitioned because it appeared to be the start of that separation of components.

Figure 10k was stretched CW but not enough to be partitioned. Figure 10l was considered bimodal, and the clockwise component in Fig. 10m was still considered distinct enough to be partitioned, but Fig. 10n was not. As a result, the H_S for the northwest propagating component jumped from 4.5 m in Fig. 10m to 5.3 m in Fig. 10n, even though the total H_S was nearly identical and the spectral shapes were very similar.

6. Storm-relative comparison of open ocean and landfall wave fields

It would be very useful to have a storm-relative model of the wave field surrounding a hurricane from which the directional wave field at any location could be determined from knowledge of the eye position and a few parameters, such as the maximum wind speed, the radii of the maximum and gale force winds, and the recent movement of the storm. Young (1999) has provided a review of the state of knowledge of hurricane wave fields prior to Wright et al. (2001) and the present paper.

Young (1997) made a detailed study of one-dimensional spectra from a quite comprehensive set of 16 hurricanes off the northwest coast of Australia. He found that the spectra were bimodal when storm centers were more than 8 times the radius of maximum winds, R, from the measurement site, and unimodal otherwise. Young (1997) concluded that the shape stabilizing effects of the nonlinear source term in the wave generation process were sufficient to continually force the spectra back to the unimodal form within $8R$ of the storm center.

The radius of maximum winds for Hurricane Bonnie was about 80 km. Most of the SRA data from 24 and 26 August 1998 are within $3R$ of the storm center and indicate complex wave fields except in the right forward quadrant of the hurricane. The SRA data suggest that the directional wave spectra for the hurricanes in Young's study were probably frequently bimodal within $8R$ of the storm center but appeared unimodal in the nondirectional spectra because the components were not sufficiently separated in frequency.

For Hurricane Bonnie the wave propagation directions showed a great similarity between open ocean and landfall, even though the maximum wind speed and translation speed had changed and the wavelength and H_S were dramatically affected by the bathymetry at landfall.

Figure 11 shows in blue, in a storm-relative reference frame, all the radials representing wave components observed during the landfall flight of 26 August 1998. Radials representing the wave components observed during the open ocean flight on 24 August 1998 are shown in red. The circles indicate the data locations, and the radials extend in the wave propagation direction a length proportional to the wavelength. The width of the radials is proportional to the H_S, so the aspect ratio is an indication of wave steepness with wide rectangles indicating steep waves.

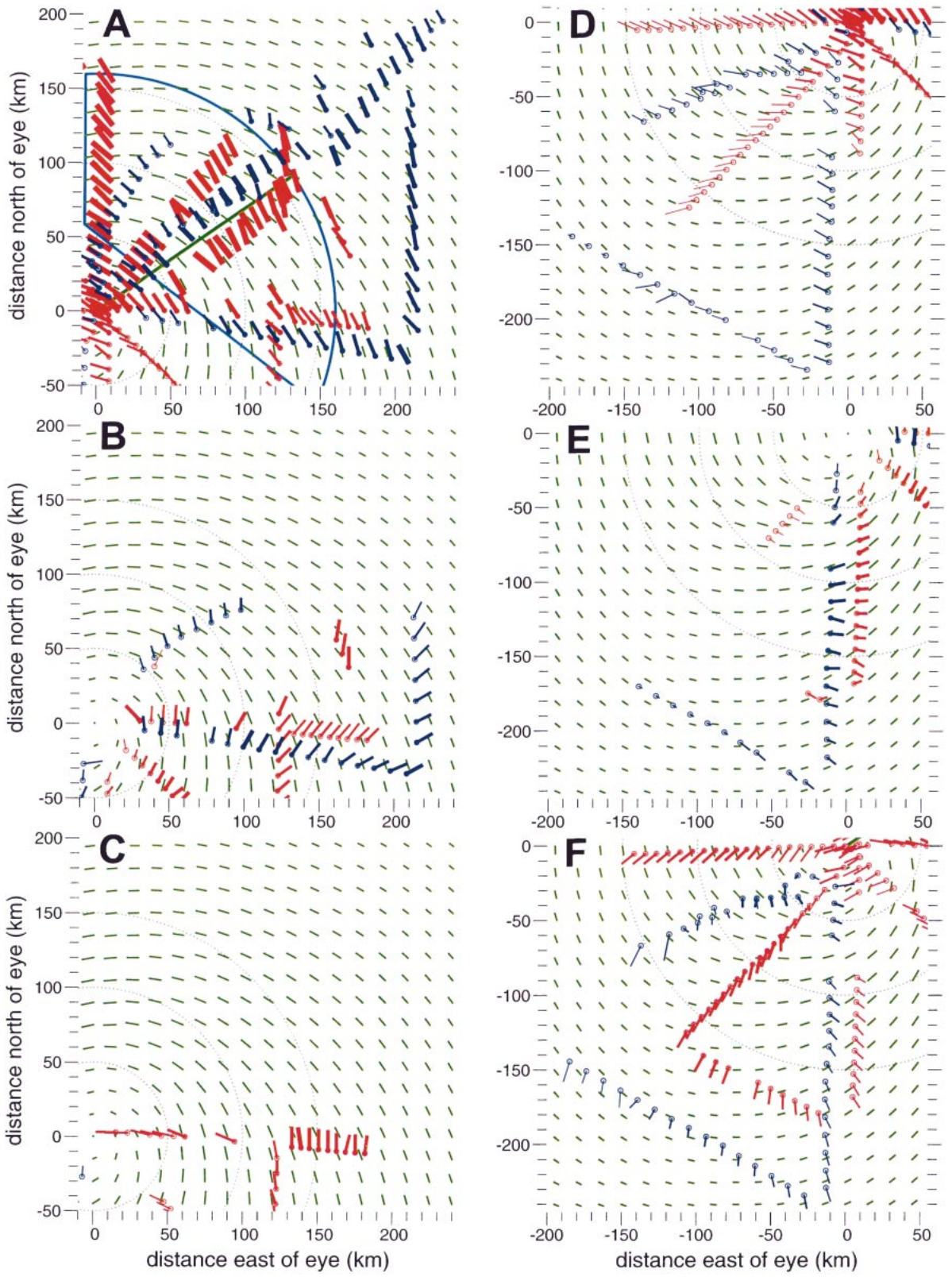

FIG. 11. Storm-relative representation of all the wave components observed during the landfall flight of 26 Aug 1998 (blue) and during the open ocean flight on 24 Aug 1998 (red). The short green radials show the average of the HRD surface wind analyses on the two days with a length of 10 km representing a wind speed of 50 m s^{-1}.

The left side of Fig. 11 focuses on the northeast quadrant of the storm. The right side of Fig. 11 focuses on the southwest quadrant. The top panels show the wave components propagating toward the northwest. The middle panels show the wave components propagating toward the northeast. The bottom panels of Fig. 11 show the wave components propagating toward the north (left side) or the south (right side). These designations should be considered approximate and were determined in the following manner.

Up to three wave components were identified in each spectrum. In the open-ocean paper (Wright et al. 2001) the components were grouped into primary, secondary, and tertiary wave fields based on wave height. For the present analysis, an initial reference direction of 315° was used, and the wave components closest to that direction were extracted and displayed in Figs. 11a and 11d. A second reference direction of 45° was used, and the remaining wave components closest to that direction were extracted and displayed in Figs. 11b and 11e. The wave components displayed in Figs. 11c and 11f were what remained after the first two iterations.

There is a remarkable agreement in the wave propagation directions for the various wave components on the two days, despite some differences in the wind fields. This agreement and the fact that wave generation involves integrals over both time and space suggests that, in spite of its complexity, the wave field in the vicinity of a hurricane may be well behaved and lend itself to be modeled by a few parameters such as the maximum wind speed, the radii of the maximum and gale force winds, and the recent movement of the storm.

The shorter wavelengths of the southward-propagating components in the southwest quadrant of Hurricane Bonnie caused by the fetch limiting at landfall are apparent in Fig. 11f. There was no tertiary wave component identified in the northeast quadrant during landfall (Fig. 11c).

The northeast quadrant of the hurricane and the waves propagating toward the northwest (Fig. 11a) will now be examined in detail. An arbitrary reference line has been added to Fig. 11a. It is the green radial extending from the center of the eye a distance of 160 km at an angle of 55° east of north. This angle was selected because it made the reference line approximately orthogonal to the general wave propagation direction in evidence in Fig. 11a, and approximately parallel to the central part of the shoreline of Onslow Bay (the region between Cape Fear and Cape Lookout).

Consider the wave vectors in Fig. 11a contained within the cyan circular and linear boundaries, relative to the green reference line. In the open ocean (red wave vectors), the wave length and height grew toward the northwest, reaching a maximum in the vicinity of the green reference line and approximately maintaining those levels northwest of the reference line.

In the region 100 km southeast of the reference line (10 km south, 150 km east in Fig. 11a), the blue wave vectors indicate that the waves in this region during landfall were longer and higher than they were in the open ocean (red radials). This may well have been because the hurricane had been moving twice as fast than it had when encountered in the open ocean.

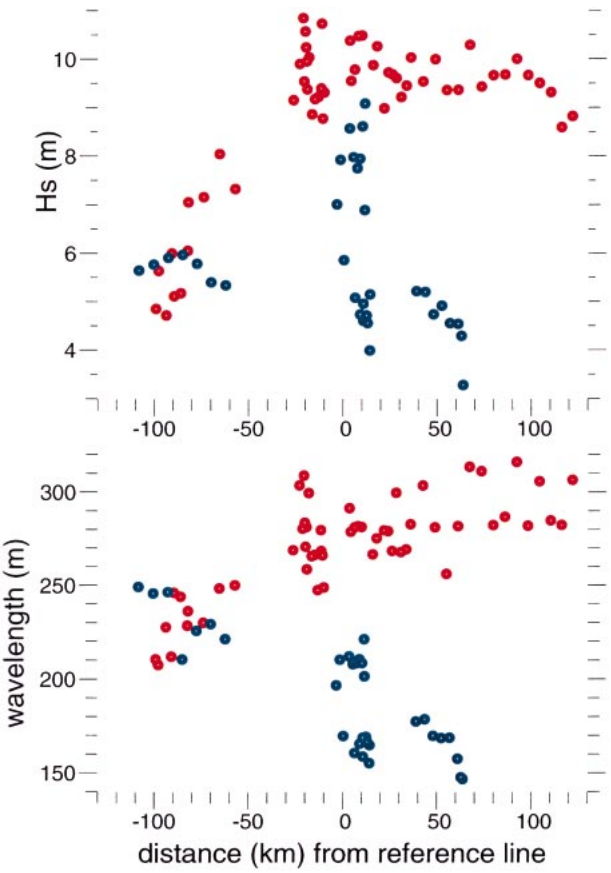

FIG. 12. Significant wave height and wavelength of the wave components within the cyan boundaries of Fig. 11a plotted with respect to their displacement northwest of the green reference line for the open ocean flight (red) and the landfall flight (blue).

In the vicinity of the green reference line in Fig. 11a, the wave height at landfall (blue) is both higher and lower than it was to the southwest of the reference line. It will become apparent that the wave height depended on how close the observations points were to the shore. Sixty kilometers northwest of the reference line (100 km N, 40 km E), the blue wave vectors, which were nearest the shoreline at landfall, are dwarfed by the red wave vectors that bracket them from the open-ocean observations.

To better quantify these impressions, the wave height and wavelength of those wave components within the cyan boundaries of Fig. 11a are plotted in Fig. 12 with respect to their displacement northwest of the green reference line. The red circles showing the open ocean data indicate that there was a rapid increase in both H_S and wavelength between -100 and -20 km. Then there was a gradual decrease in H_S and a gradual increase in wave-

length as the distance northwest of the reference line increased. This is to be expected for swell propagating away from the hurricane under the influence of a wind that was diminishing and turning more and more away from the downwave direction (Fig. 11a).

Considering the larger initial values of H_S and wavelength 100 km southeast of the reference line for the landfall (blue) data, those quantities might have reached 10 and 300 m, respectively, in the vicinity of the reference line had it not been for the bathymetry. The blue circles in Fig. 12 demonstrate the large span in H_S in the vicinity of the reference line with values both larger and smaller than those for 100 km southeast of the reference line. The wavelength was smaller in the vicinity of the reference line than it was 100 km southeast of it, but there was still a large range of values in that region.

7. Bathymetric effect on wave field

Ideal conditions for studying the influence of bathymetry on waves would be a quasi-steady state, where the wind generation and nonlinear interaction of the waves could be neglected. The present dataset consists of steep waves driven by a high wind that was changing rapidly. A rigorous analysis of these data is beyond the scope of this paper, but several simple approaches will be used to demonstrate the bathymetric influence.

Figure 13 demonstrates the shortening of the wavelength and the lowering of the wave height when the waves approach the shore. It shows the North Carolina coast from Cape Lookout to Cape Fear and SRA northwest wave vectors from three passes of the NOAA aircraft. As in Fig. 11, the circles indicate the data locations. The radials extend in the wave propagation direction a length proportional to the wavelength with their width proportional to H_S.

The red wave vectors were from the initial pass with the aircraft flying toward the northeast about 70 km from shore. The blue wave vectors were from a pass toward the southwest much closer to shore about an hour later.

The two blue wave vectors bracketing Cape Lookout (34.58°N, 76.53°W) in Fig. 13 correspond to the wave topography of Fig. 4 and the spectra of Figs. 7j and 7k. They and the wave vector just to the west of them in Fig. 13 appear in Fig. 11a just outside the cyan circle at about 125 km N. The blue wave vectors starting near the middle of the Onslow Bay shoreline (34.52°N, 77.32°W) in Fig. 13 and progressing toward the southwest are in evidence in Fig. 11a starting at 112 km N, 50 km E.

The time associated with the Fig. 13 wave vector at 33.66°N, 77.35°W (Fig. 6k) was 61630 sod. The time associated with the blue location that the red wave vector of Fig. 6k points toward (34.01°N, 77.76°W; Fig. 7o) was 66467 sod, about 1 h, 21 min after the red observation. The thin radials in Fig. 13 show the HRD surface winds corresponding to the eye locations for the two times just indicated, with a wind speed of 40 m s^{-1} corresponding to a length of 0.05° of latitude.

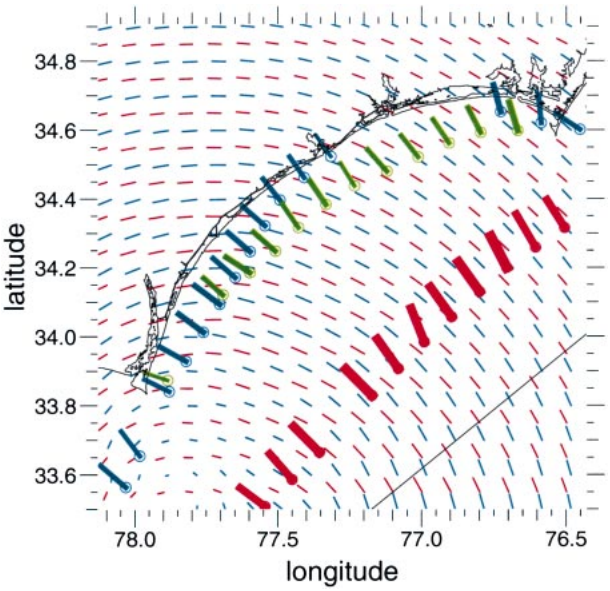

FIG. 13. North Carolina coast from Cape Fear (33.83°N, 77.96°W) to Cape Lookout (34.58°N, 76.53°W) and thick radials (red, blue, green) showing SRA northwest wave vectors from three passes of the NOAA aircraft. The radials extend in the wave propagation direction a length proportional to the wavelength. The width of the radials is proportional to H_S. The thin red and blue radials show the HRD surface wind analysis for times corresponding to the red and blue passes. The diagonal line in the lower right corner is part of the piecewise linear representation of the north wall of the Gulf Stream shown in the plan views of Figs. 6–10.

The dominant wavelength of the red wave vector (Fig. 6k) was 210 m, and H_S was 7.9 m. For the corresponding blue wave vector (Fig. 7o), the wavelength was reduced to 177 m, and H_S was 5.2 m. The group velocity of waves of length 210 m is 9.05 m s^{-1}, which would require 1 h, 39 min to travel the 54 km distance between those two positions. Had the water been deep, the time difference between the two observations was such that one would almost be observing a later manifestation of the same group of waves. The wind was blowing very strongly at an angle of about 30° with respect to the line joining the two observations (downwave direction for Fig. 6k). It was initially about 38 m s^{-1} and decreased to about 30 m s^{-1} by the time of the blue observation due to the movement of the storm and the large wind gradient inside the radius of maximum wind. In the absence of the dissipation caused by the bathymetry, it is apparent that both the wavelength and wave height would have increased between the red and blue observations.

The disparity is even greater if one considers the red wave vector in Fig. 13 at 33.83°N, 77.17°W (Fig. 6l) and the corresponding blue wave vector at 34.25°N, 77.60°W (Fig. 7n). The red dominant wavelength (Fig. 6l) was 212 m, and H_S was 8.6 m. For Fig. 7n, the wavelength was reduced to 168 m, and H_S was 4.9 m,

even though the wind over the region between them was approximately constant at about 39 m s^{-1} and was only about 25° off the downwave direction. The larger initial waves and stronger wind could not compensate for the second blue observation point being closer to shore in more shallow water.

The incremental wave growth analysis of Donelan et al. (1992) suggests about a 10% increase in the wavelength and wave height in the first example, just discussed, and about a 15% increase in the second. The observed values were 16% and 21% reductions in wavelength in the two examples, with 34% and 43% reductions in the wave height.

The green wave vectors in Fig. 13 were from another pass toward the southwest near the end of the dataset. The wave vector at 34.56°N, 76.90°W (Fig. 10k) was at 80261 sod, about 5 h after the spectrum Fig. 6m of the red pass whose corresponding wave vector was 55 km directly south of it at 34.06°N, 76.90°W. Figure 10k had a wavelength of 165 m, and H_S was 5.8 m versus wavelength 210 m and H_S 7.9 m for Fig. 6m. This demonstrates even more strongly the bathymetric dissipation of the waves since these two spectra were coincident at 73 km N, 89 km E of the eye in a storm-relative reference frame. In general, the flight lines producing the green and red wave vectors in Fig. 13 were nearly coincident in a storm-relative reference frame (in the vicinity of the green reference line in Fig. 11a), producing the large span in H_S and wavelength near the zero abscissa value in Fig. 12.

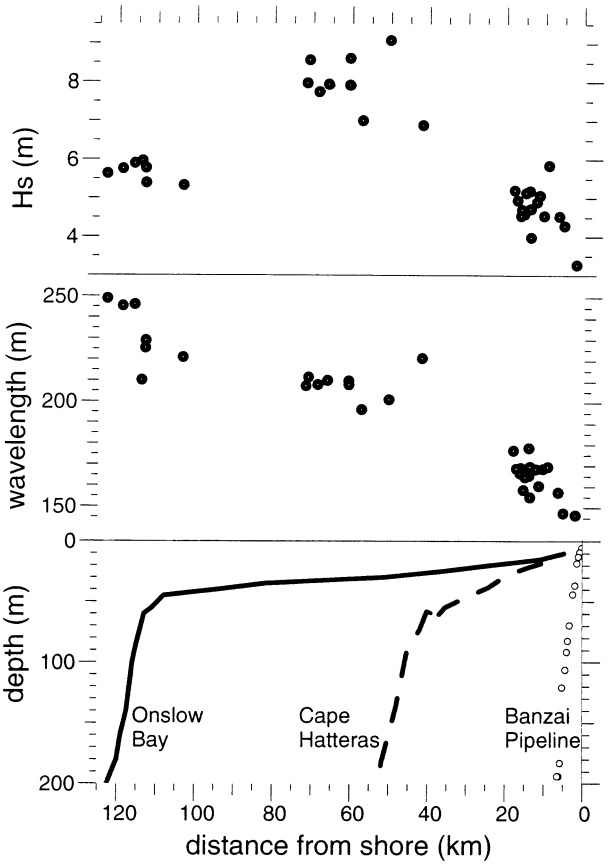

FIG. 14. Landfall data from Fig. 12 plotted vs distance from shore in Onslow Bay. The bottom panel plots the approximate bathymetric profiles for Onslow Bay, the northward flight line toward Cape Hatteras (Fig. 5), and the Banzai Pipeline on the northwest shore of Oahu, Hawaii.

8. Shoreline-relative wave field variation

Figure 14 plots the same landfall data shown in Fig. 12 but versus the distance from shore. A piecewise linear approximation to the shoreline of Onslow Bay, located between Cape Fear and Cape Lookout, was used to compute the minimum distance to the shoreline for each observation point. In this representation, the data show a much less erratic variation. The contours of constant water depth in Onslow Bay approximately follow the shoreline. The solid curve in the bottom panel of Fig. 14 shows the water depth variation along a line perpendicular to the shoreline starting from about 34.53°N, 77.33°W.

Figure 14 shows that the wavelength begins to shorten as soon as the waves encounter the continental shelf, and the effect becomes more pronounced as the depth decreases near shore. The wave height continues to grow on the shelf until about 50 km from shore, where the bathymetry gradient steepens, and the strong winds can no longer overcompensate for the dissipation effects. The data gaps in the 20–40 km and 75–100 km distances from shore occurred because the flight lines generally tended to parallel the shoreline during the landfall flight.

For perspective, two other bathymetric profiles are shown in the bottom panel of Fig. 14. The dashed curve shows the depth variation along the northward flight line toward Cape Hatteras (Fig. 5). That flight line provided continuous data versus distance from shore, but was not used to demonstrate the bathymetric effect because there was also a wave height gradient along the flight line due to the aircraft moving away from the eye (Fig. 3).

The third bathymetric profile, indicated by the circles in the bottom panel of Fig. 14, is for the Banzai Pipeline, the fabled surfing area on the northwest coast of Oahu, Hawaii. It is apparent why that region has the gigantic plunging breaking waves that make it famous. The bathymetry is such that the incoming swell does not feel the bottom until it is only about 3 or 4 km from shore where the shoaling occurs abruptly. There is no time or space for a gradual dissipation of the wave energy so the swell rears up into the huge plunging breakers seen in the surfing and travel magazines. The continental shelf of most of the U.S. Mid-Atlantic and Gulf of Mexico coasts prevents the occurrence of a similar situation there.

In discussing the approximations for deep and shallow water waves, Kinsman (1965, p. 130) developed an

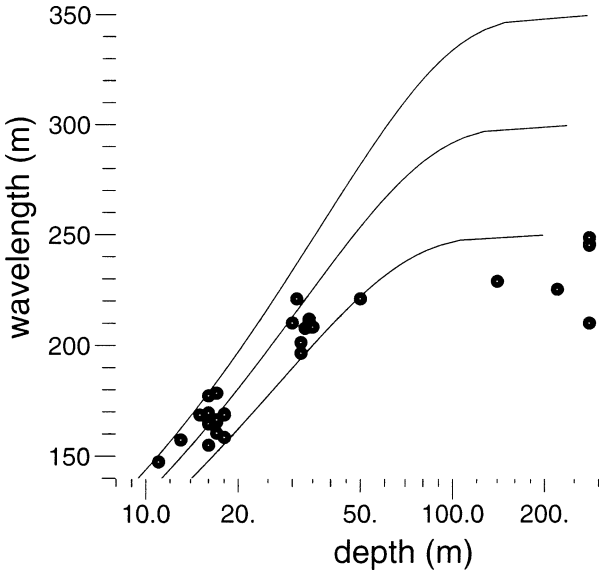

FIG. 15. Curves show expected variation of swell wavelength vs water depth for three values of deep water wavelength: 250 m, 300 m, and 350 m. The wavelength data from Fig. 14 are plotted (circles) vs water depth at the observation locations extracted from the NGDC bathymetric database.

expression for the ratio of a swell wavelength L in any water depth h to its wavelength L_d in deep water:

$$L_d^{-1} L = \tanh[\kappa_d h(L_d^{-1} L)^{-1}], \quad (2)$$

where κ_d is the deep water wavenumber. He pointed out that there is no analytic solution to (2), but that it can be solved numerically by assigning various values to $L_d^{-1} L$ and solving for the corresponding values of $\kappa_d h$. Figure 15 plots the resulting values of wavelength L versus water depth for three values of deep water wavelength L_d: 250 m, 300 m, and 350 m. The circles are the wavelength data from Fig. 14 versus water depth at the observation location extracted from the National Geophysical Data Center (NGDC) bathymetric data base (Coastal Relief Model, Vol. 2, U.S. South East Atlantic Coast), which is referenced to mean sea level.

The SLOSH model (Jelesnianski et al. 1992) indicated (W. Shaffer 2001, personal communication) that storm surge from Hurricane Bonnie increased the water depth up to 2 m within about 5 km from shore (water depths of 10 m or less). This effect would have been minimal for the data points shown in Fig. 15 and storm surge was not incorporated in them.

The observed deep water wavelength was in the range 200 to 250 m, but the data are spread between the 250-m and 300-m wavelength curves at 30-m water depth, and between the 250-m and 350-m curves at depth 10 to 20 m. This is a reasonable result considering that the waves were strongly forced, and the wavelength would have been growing as the shoreline was approached had it not been for the bathymetric effect.

9. Conclusions

The spatial variation of the direction of propagation of the various components of the complex directional wave spectrum of Hurricane Bonnie showed a remarkable similarity in open ocean and while making landfall near Wilmington, North Carolina. This suggests that the hurricane wave field may be a well-behaved function of a few simple parameters such as the maximum wind speed, the radii of maximum and gale-force winds, and the recent motion of the eye. The hurricane wave height during landfall was modified dramatically by the continental shelf. The open ocean data suggested that the significant wave height on the coast northeast of Wilmington would have been 10 m in the absence of the shelf. The actual wave height observed 5 km from shore was about 4 m. The bathymetry distributed the wave dissipation process across the shelf, so that the wavelength and wave height were reduced gradually as the shore was approached.

Acknowledgments. Donald E. Hines of EG&G, Inc. maintained the SRA, and Gerald S. McIntire of CSC installed it in NOAA aircraft N43RF. The authors thank the flight crew and staff of the NOAA/AOC for their help in ensuring the success of this experiment. The Science and Engineering Division deserves special recognition for work in installing the SRA on N43RF and developing the needed interfaces with the other aircraft systems. This work was supported by the NASA Solid Earth/Natural Hazards Program, the NASA Physical Oceanography Program, and the Office of Naval Research (Document Number N00014-98-F-0209 and the CBLAST DRI Program Element 601153N).

REFERENCES

Ardhuin, F., T. H. C. Herbers, and W. C. O'Reilly, 2001: A hybrid Eulerian–Lagrangian model for spectral wave evolution with application to bottom friction on the continental shelf. *J. Phys. Oceanogr.,* **31,** 1498–1516.

Avila, L. A., cited 1998: Preliminary report: Hurricane Bonnie 19–30 August 1998. NOAA National Hurricane Center/Tropical Prediction Center. [Available online at http://www.nhc.noaa.gov./1998bonnie.html.]

Banner, M. L., A. V. Babanin, and I. R. Young, 2000: Breaking probability for dominant waves on the sea surface. *J. Phys. Oceanogr.,* **30,** 3145–3160.

Bowyer, P. J., 2000: Phenomenal waves with a transitioning tropical cyclone, Luis, the Queen, and the buoys. Preprints, *24th Conf. on Hurricanes and Tropical Meteorology,* Ft. Lauderdale, FL, Amer. Meteor. Soc., 294–295.

Bretschneider, C. L., 1957: Hurricane design wave practices. ASCE, *J. Waterw. Harbor Div.,* **83,** 1238-1–1238-33.

Donelan, M., M. Skafel, H. Graber, P. Liu, D. Schwab, and S. Venkatesh, 1992: On the growth of wind-generated waves. *Atmos.–Ocean,* **30,** 457–478.

Hasselmann, K., and Coauthors, 1973: Measurements of wind-wave growth and swell decay during the Joint North Sea Wave Project (JONSWAP). *Deut. Hydrogr. Z.,* **A8** (12) (Suppl.), 95 pp.

Hwang, P. A., E. J. Walsh, W. B. Krabill, R. N. Swift, S. S. Manizade, J. F. Scott, and M. D. Earle, 1998: Airborne remote sensing ap-

plications to coastal wave research. *J. Geophys. Res.*, **103,** 18 791–18 800.

Jelesnianski, C. P., J. Chen, and W. A. Shaffer, 1992: SLOSH: Sea, lake, and overland surges from hurricanes. NOAA Tech. Rep. NWS 48, 71 pp. [Available from NOAA/MDL W/OST25, 1325 East–West Hwy., Silver Spring, MD 20910.]

Kinsman, B., 1965: *Wind Waves.* Prentice Hall, 676 pp.

MacAfee, A. W., and P. J. Bowyer, 2000a: Trapped-fetch waves in a transitioning tropical cyclone (Part I—The need and the theory). Preprints, *24th Conf. on Hurricanes and Tropical Meteorology,* Ft. Lauderdale, FL, Amer. Meteor. Soc., 292–293.

——, and ——, 2000b: Trapped-fetch waves in a transitioning tropical cyclone (Part II—Analytical and predictive model). Preprints, *24th Conf. on Hurricanes and Tropical Meteorology,* Ft. Lauderdale, FL, Amer. Meteor. Soc., 165–166.

Powell, M. D., S. H. Houston, and T. A. Reinhold, 1996: Hurricane Andrew's landfall in south Florida. Part I: Standardizing measurements for documentation of surface wind fields. *Wea. Forecasting,* **11,** 304–328.

Shemdin, O. H., 1980: Prediction of dominant wave properties ahead of hurricanes. *Proc. 17th Int. Coastal Engineering Conf.,* Sydney, Australia, ASCE, 600–609.

——, K. Hasselmann, S. V. Hsiao, and K. Herterich, 1978: Nonlinear and linear bottom interaction effects in shallow water. *Turbulent Fluxes through the Sea Surface, Wave Dynamics, and Prediction,* A. Favre and K. Hasselmann, Eds., Plenum, 347–372.

Tolman, H. L., 1994: Wind waves and moveable-bed bottom friction. *J. Phys. Oceanogr.,* **24,** 994–1009.

Walsh, E. J., D. W. Hancock, D. E. Hines, R. N. Swift, and J. F. Scott, 1985: Directional wave spectra measured with the surface contour radar. *J. Phys. Oceanogr.,* **15,** 566–592.

——, ——, ——, ——, and ——, 1989: An observation of the directional wave spectrum evolution from shoreline to fully developed. *J. Phys. Oceanogr.,* **19,** 670–690.

——, L. K. Shay, H. C. Graber, A. Guillaume, D. Vandemark, D. E. Hines, R. N. Swift, and J. F. Scott, 1996: Observations of surface wave-current interaction during SWADE. *Global Atmos. Ocean Syst.,* **5,** 99–124.

Wright, C. W., and Coauthors, 2001: Hurricane directional wave spectrum spatial variation in the open ocean. *J. Phys. Oceanogr.,* **31,** 2472–2488.

Young, I. R., 1988: Parametric hurricane wave prediction model. ASCE *J. Waterw. Port, Coastal, Ocean Eng.,* **114,** 637–652.

——, 1997: Observations of the spectra of hurricane generated waves. *Ocean Eng.,* **25,** 261–276.

——, 1999: *Wind Generated Ocean Waves.* Elsevier, 288 pp.

——, and R. M. Gorman, 1995: Measurements of the evolution of ocean wave spectra due to bottom friction. *J. Geophys. Res.,* **100,** 10 987–11 004.